Materials Science & Engineering A 942 (2025) 148642

Contents lists available at ScienceDirect

Materials Science & Engineering A

journal homepage: www.elsevier.com/locate/msea

Harnessing competitive interplay between precipitation and lattice distortion for strong and ductile medium-entropy alloy

Jae Heung Lee [a], Hyeonseok Kwon [b,*], Gang Hee Gu [a], Ji Yeong Lee [a], Sang Guk Jeong [c], Emad Maawad [d], Changwan Ha [e], Jaemin Wang [b], Byeong-Joo Lee [a], Sangbong Yi [f,**], Takayoshi Nakano [g], Hyoung Seop Kim [a,c,h,i,***]

[a] Department of Materials Science and Engineering, Pohang University of Science and Technology (POSTECH), Pohang, 37673, Republic of Korea
[b] Center for Advanced Aerospace Materials, Pohang University of Science and Technology (POSTECH), Pohang, 37673, Republic of Korea
[c] Advanced Institute for Materials Research (WPI-AIMR), Tohoku University, Sendai, 980-8577, Japan
[d] Helmholtz-Zentrum Hereon, Institute of Materials Physics, Max-Planck-Str. 1, Geesthacht, 21502, Germany
[e] Pohang Accelerator Laboratory, Pohang University of Science and Technology (POSTECH), Pohang, 37673, Republic of Korea
[f] School of Materials Science and Engineering, Kumoh National Institute of Technology, Gumi, 39177, Republic of Korea
[g] Division of Materials and Manufacturing Science, Graduate School of Engineering, The University of Osaka, 565-0871, Japan
[h] Graduate Institute of Ferrous & Eco Materials Technology, Pohang University of Science and Technology (POSTECH), Pohang, 37673, Republic of Korea
[i] Center for Heterogenic Metal Additive Manufacturing, Pohang University of Science and Technology (POSTECH), Pohang, 37673, Republic of Korea

ARTICLE INFO

Keywords:
Ferrous medium-entropy alloy
Precipitation
Deformation mechanism
Strengthening mechanism
In-situ synchrotron X-ray diffraction

ABSTRACT

In Co-Cr-Fe-Ni-Mo-C ferrous medium-entropy alloys (FeMEAs), precipitation-driven alteration of matrix composition affects both the kinetics of deformation-induced martensitic transformation (DIMT) and the degree of lattice distortion. While DIMT has been well studied, the role of lattice distortion remains explored. In this study, we simultaneously enhance the strength and ductility in $Co_{18}Cr_{13}Fe_{57.5}Ni_{7.5}Mo_3C_1$ (at%) FeMEA by harnessing the competitive interplay between precipitation and lattice distortion. Two annealed samples with similar grain sizes but different precipitate characteristics were prepared. The sample with suppressed precipitation exhibits improved ductility while maintaining comparable strength. The two specimens exhibited similar yield strengths due to a trade-off between precipitation strengthening and solid solution strengthening. However, the sample with higher lattice distortion and reduced precipitation demonstrates superior strain-hardening behavior owing to the lattice distortion-induced back stress, acting as an effective strain-hardening mechanism, and delayed DIMT, serving as a ductilizing mechanism. This work offers a strategy to modulate strengthening and deformation mechanisms in Co-Cr-Fe-Ni-Mo-C FeMEAs via precipitation control.

1. Introduction

High-entropy alloys (HEAs) have attracted the attention of many researchers since their emergence. Traditionally, the excessive addition of solute elements was believed to result in the formation of brittle intermetallic compounds, hindering various alloy design attempts for structural materials. However, HEAs have demonstrated the ability to maintain a single-phase structure due to the high-entropy effect, and furthermore, exhibit excellent mechanical properties, opening a new window in alloy design [1-3]. Currently, the concept has expanded to include medium-entropy alloys (MEAs) with relatively lower configuration entropy owing to fewer constituent elements or non-equiatomic compositions.

To enhance mechanical properties, research aimed at incorporating a transformation-induced plasticity (TRIP) effect has been actively performed [4,5]. In particular, ferrous MEAs (FeMEAs) are alloys designed to induce deformation-induced martensitic transformation (DIMT) from face-centered cubic (FCC) to body-centered cubic (BCC) by varying the Fe content, exhibiting exceptional strain-hardening capabilities due to the superior load-bearing capacity of the newly-born BCC martensite

* Corresponding author.
** Corresponding author.
*** Corresponding author. Department of Materials Science and Engineering, Pohang University of Science and Technology (POSTECH), Pohang, 37673, Republic of Korea.
E-mail addresses: hyunsug007@postech.ac.kr (H. Kwon), sangbong.yi@kumoh.ac.kr (S. Yi), hskim@postech.ac.kr (H.S. Kim).

https://doi.org/10.1016/j.msea.2025.148642
Received 24 March 2025; Received in revised form 31 May 2025; Accepted 4 June 2025
Available online 5 June 2025

[6-8]. Additionally, their high Fe content provides cost-effectiveness, making them a promising alloy for future structural applications [9].

Recently, we have developed FeMEAs by introducing precipitation strengthening through the addition of Mo and C, with the aim of further increasing their strength [10-17]. The advanced Co-Cr-Fe-Ni-Mo-C FeMEAs are characterized by significant carbide precipitation during heat treatment, due to Mo serving as a strong carbide former, inducing precipitation strengthening. Along with precipitation, the composition of the FCC matrix also changes, and previous studies have demonstrated that the alteration in the composition of the FCC matrix has a significant impact on metastability [10,12,15,16]. More intensive precipitation leads to a further reduction in the phase stability of the FCC matrix, resulting in a more pronounced DIMT. As a result, the strength increased, but it was also accompanied by a decrease in ductility.

Changes in the matrix composition owing to carbide precipitation not only impact TRIP kinetics but also affect the degree of lattice distortion. According to the research by Li et al. [18] and Wang et al. [19], greater addition of Mo or C into the FCC matrix results in a more pronounced degree of lattice distortion. Therefore, while active precipitation boosts TRIP kinetics, it can also diminish the degree of lattice distortion by decreasing the contents of Mo and C in the FCC matrix. Since severe lattice distortion in HEAs or MEAs is known to enhance slip planarity and increase back stress [20,21], active precipitation in Co-Cr-Fe-Ni-Mo-C FeMEAs consequently has the drawback of weakening back stress. This implies that there is a competitive interplay between precipitation and lattice distortion in deformation mechanisms. We have primarily focused on controlling the TRIP effect and have not extensively addressed the lattice distortion-induced back stress. We thus suggest that there remains a potential for further improvement in the mechanical properties of Co-Cr-Fe-Ni-Mo-C FeMEAs through careful control of competitive effects between precipitation and lattice distortion.

In this study, we aim to enhance the tensile properties of fully recrystallized $Co_{18}Cr_{13}Fe_{57.5}Ni_{7.5}Mo_3C_1$ (at%) FeMEA via precipitation and lattice distortion control, which influence both strengthening mechanisms, such as precipitation strengthening and solid solution strengthening, and deformation mechanisms, such as DIMT and back stress. Two different annealing conditions of 800°C for 3 h and 900°C for 10 min were used to vary precipitation while maintaining a constant grain size, in order to isolate the effect of grain size and verify only the effects of precipitation and lattice distortion on tensile properties. A specimen annealed at 900°C demonstrated greater ductility compared to its counterpart annealed at 800°C without compromising strength, and we provide detailed discussions on their strengthening and deformation mechanisms, based on microstructural characterization and in-situ synchrotron X-ray diffraction study.

2. Experimental method

2.1. Alloy fabrication

$Co_{18}Cr_{13}Fe_{57.5}Ni_{7.5}Mo_3C_1$ (at%) FeMEA was cast using the vacuum induction melting method. All elements used for casting were of at least 99.9 % purity. The ingot was homogenized at 1100°C for 6 h under an argon atmosphere, followed by water-quenching. The homogenized ingot was then cold-rolled at room temperature. The thickness reduction ratio was ~86 % (from 7.0 to 1.0 mm). The cold-rolled sheet was annealed under two distinct conditions to control precipitation without altering the grain size: at 800°C for 3 h (A800) and at 900°C for 10 min (A900). All annealed samples were subjected to water quenching.

2.2. Mechanical testing

Dog-bone-shaped tensile specimens ($1.0 \times 2.5 \times 6.4$ mm^3) were cut from the annealed sheet along the rolling direction. Uniaxial tensile tests were performed at a strain rate of 1×10^{-3} s^{-1} using a universal testing machine (Instron 5582, Instron Corp., USA). All uniaxial tensile tests were repeated 3 times. Loading-unloading-reloading (LUR) tests were conducted using the same universal testing machine at the same strain rate. The digital image correlation (ARAMIS M12, GOM Optical Measuring Techniques, Germany) technique was utilized during the uniaxial tensile and LUR tests for accurate measurements of elongation and local strain. All specimens were sprayed with white and black paint prior to the tensile tests.

2.3. Microstructural characterization

For microstructural analyses, each sample was mechanically polished using SiC papers (up to 1200-grit), followed by electrochemical polishing with a 92 % CH_3COOH + 8 % $HClO_4$ solution. Electron backscatter diffraction (EBSD) and electron channeling contrast imaging (ECCI) analyses were conducted using a field-emission scanning electron microscope (FE-SEM) (JSM-7900 F, JEOL, Japan). The obtained EBSD data were interpreted using orientation imaging microscopy (OIM) analysis software (TSL OIM analysis 7). Backscatter electron (BSE) images were obtained using the same FE-SEM. Scanning transmission electron microscopy (STEM) analyses were performed using a transmission electron microscope (TEM) (JSM-2100 F, JEOL, Japan) equipped with an energy dispersive X-ray (EDS) detector. Thin foil samples for STEM analysis were prepared using a dual-beam focused ion beam (FIB) (FEI Helios Nano-Lab™).

2.4. In-situ synchrotron X-ray diffraction

In-situ synchrotron XRD tests were conducted during uniaxial tensile testing on both A800 and A900 specimens, each with a gauge geometry of $1.0 \times 4.0 \times 15.0$ mm^3, at the P07 High Energy Materials Science Beamline of Petra III in Deutsches Elektronen-Synchrotron (DESY, Germany). For each sample, six diffraction patterns were obtained intermittently through load control in the elastic region. In the plastic region, diffraction patterns were acquired discontinuously using the strain control method with a crosshead speed of 0.9 mm/min, which corresponds to a strain rate of 1×10^{-3} s^{-1}. A high-energy synchrotron beam (87 keV, wavelength of 0.14032 Å, size of 700×700 μm^2) was employed, allowing the in-situ synchrotron XRD tests to be conducted in transmission mode. A panel detector (PerkinElmer Inc., USA) with 2048 × 2048 pixels (size of 200×200 μm^2) was used to collect diffracted 2-dimensional Debye-Scherrer rings, which were caked along the loading direction (azimuthal angle range from 82.5° to 97.5°) and integrated into 1-dimensional XRD line profiles using Fit2D software [22]. The sample-to-detector distance, determined using LaB_6 powder diffraction data, was 1251.113 mm. The position and intensity of each peak were determined through single peak fitting, using a pseudo-Voigt function [22,23].

3. Results

3.1. Initial microstructure

XRD line profiles in Fig. 1(a) reveal that both A800 and A900 have an FCC matrix. The lattice parameters of both alloys are ~0.3580 nm and ~0.3583 nm, respectively. The Williamson-Hall method was applied to the XRD line profiles to quantify the lattice distortion and dislocation density in both samples [24,25]. The lattice distortion (ε) was calculated using the following equation [26]:

$$\beta \cos\theta = 4\varepsilon \sin\theta + \frac{k\lambda}{D_c}, \quad (1)$$

where β is the full width at half maximum (FWHM), $k = 0.9$ is a shape factor, $\lambda = 0.14032$ Å is the wavelength, and D_c is the crystallite size. Linear fitting of $\beta \cos\theta$ versus $4 \sin\theta$ yields lattice distortion values of

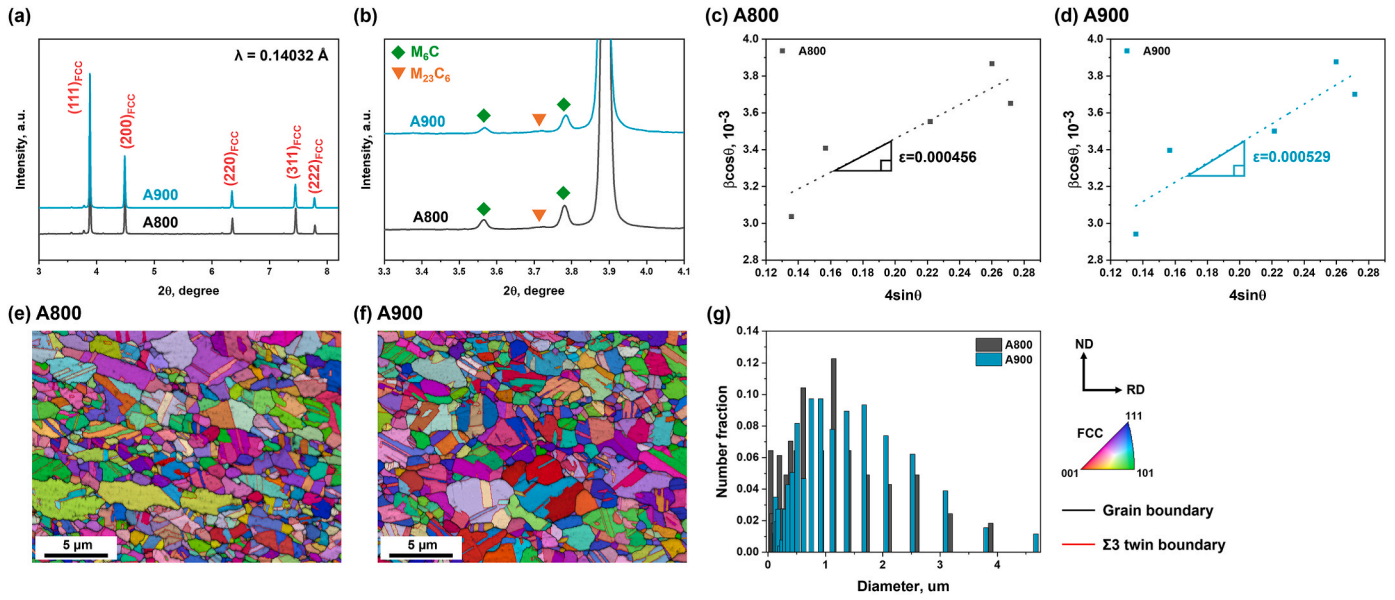

Fig. 1. (a) Synchrotron XRD line profiles of A800 and A900 taken prior to tensile loading and (b) an enlarged section of the 2θ range from 3.3° to 4.1°. The plots of $\beta \cos\theta$ versus $4 \sin\theta$ for (c) A800 and (d) A900. EBSD IQ + IPF maps of (e) A800 and (f) A900. (g) Grain size distributions of A800 and A900.

0.000456 for A800 and 0.000529 for A900, respectively (Fig. 1(c) and (d)). Additionally, the dislocation density (ρ) was estimated using the following equation [25]:

$$\rho = k_0 \frac{\varepsilon^2}{b^2}, \tag{2}$$

where $k_0 = 1.61$ is a constant for the FCC phases and b is the magnitude of the Burgers vector of each sample. A800 and A900 exhibit comparable dislocation densities of ~5.2×10^{13} m^{-2} and ~7.0×10^{13} m^{-2}, respectively, which are similar to that in fully recrystallized fine-grained FCC FeMEA [25]. EBSD inverse pole figure (IPF) maps overlaid on image quality (IQ) maps (Fig. 1(e) and (f)) demonstrate that the FCC matrix of both alloys exhibits similar characteristics. As shown in Fig. S1 (Supplementary Material), grains with grain orientation spread (GOS) values exceeding 2° are negligible in both samples, and since recrystallized grains are typically characterized by GOS values below 2° [12,15], it is evident that both samples are fully recrystallized. In addition, they exhibit similar average grain sizes and grain size distributions: 2.36 ± 1.06 μm for A800 and 2.53 ± 1.17 μm for A900. Abundant annealing twin boundaries are also observed in both alloys. The twin boundary fractions of A800 and A900 are 0.48 and 0.54, respectively. In addition, M_6C and $M_{23}C_6$ carbide peaks are shown in Fig. 1(b), indicating that carbide precipitation occurs. BSE images (Fig. 2(a) and (b)) provide a comparative view of the size and distribution of carbides in both alloys. It can be seen that A800 has more abundant and coarse carbide precipitates than A900. The more active precipitation observed in A800 is due to the lower annealing temperature, which provides a higher driving force for precipitation [27,28].

Quantitative nano-scale analyses of carbide precipitates and the chemical compositions of the FCC matrix were performed using TEM. STEM-EDS maps of both alloys in Fig. 3 reveal the presence of two types of carbides: Mo-rich and Cr-rich carbides. Based on our previous studies of Co-Cr-Fe-Ni-Mo-C FeMEAs [10-12], these correspond to M_6C and $M_{23}C_6$ carbides, as confirmed by the XRD line profiles (Fig. 1(b)). Each carbide particle was analyzed using image J software. By combining the thresholding function with manual refinement of the segmentation, individual particles were clearly distinguished from the FCC matrix (Fig. S2 in the supplementary material). Each particle was subsequently identified as either a Mo-rich M_6C carbide or a Cr-rich $M_{23}C_6$ carbide by comparison with the corresponding EDS maps. The area fractions and average radii of the two types of carbides in each sample are listed in Table 1. Both M_6C and $M_{23}C_6$ carbides in A800 exhibit a higher area

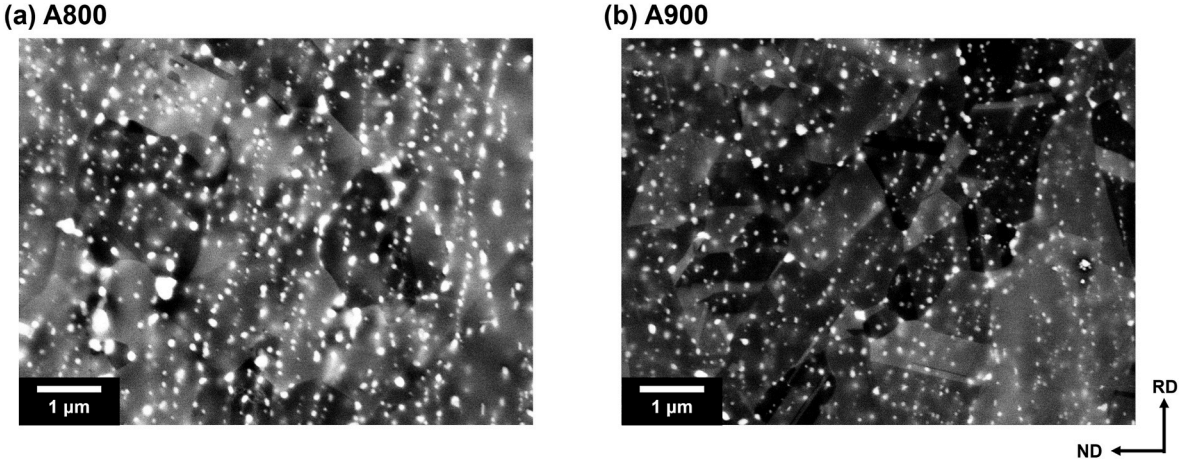

Fig. 2. BSE images of (a) A800 and (b) A900.

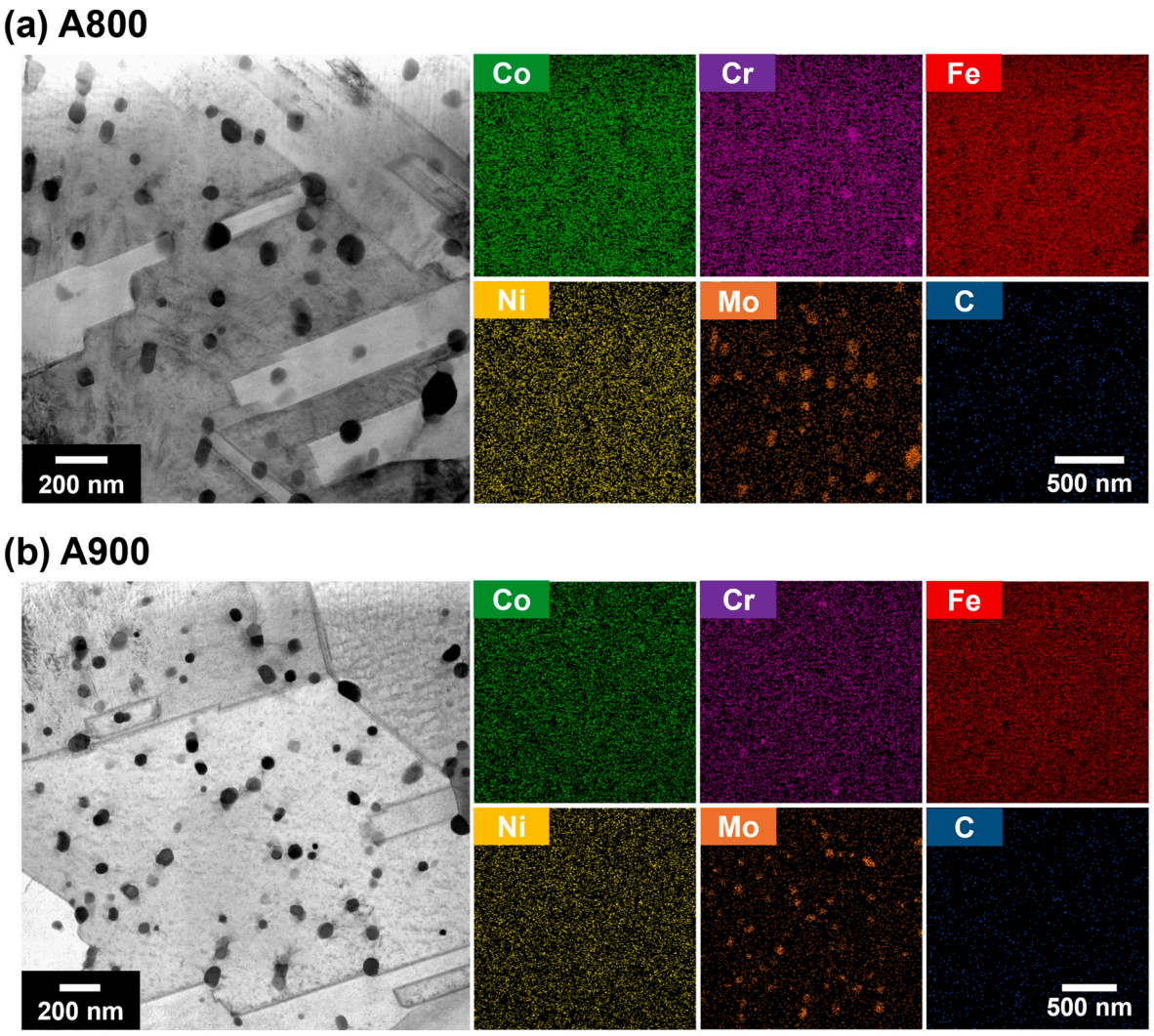

Fig. 3. STEM and EDS maps of (a) A800 and (b) A900.

Table 1
The area fractions and average radii of M_6C and $M_{23}C_6$ carbides in A800 and A900.

		Area fraction	Average radius
A800	M_6C	~6.16 %	~34.45 nm
	$M_{23}C_6$	~0.69 %	~35.05 nm
A900	M_6C	~4.11 %	~26.12 nm
	$M_{23}C_6$	~0.56 %	~30.54 nm

fraction and larger average radius compared to those in A900. This observation aligns with the trend identified in the BSE analysis. The chemical compositions of the FCC matrix in both alloys were also characterized using STEM-EDS analysis (Table 2). The compositions of Co, Cr, Fe, Ni, and Mo in the FCC matrix were determined through at least five-point EDS analyses. Contrary to these heavy elements, the composition of C was challenging to ascertain via EDS analysis. The C content in the FCC matrix was estimated using the following proportional equation [12]:

Table 2
Comparison of the experimentally obtained and the thermodynamically calculated compositions of the FCC matrix in A800 and A900.

		Co [at %]	Cr [at %]	Fe [at %]	Ni [at %]	Mo [at %]	C [at %]
A800	Exp.	18.71	14.49	58.24	6.41	2.10	0.05
	Calc.	18.80	11.86	59.61	7.91	1.76	0.05
A900	Exp.	18.96	14.49	57.30	6.18	2.71	0.36
	Calc.	18.65	12.12	59.19	7.84	2.00	0.20

$$\left\{\frac{n^C_{FCC}}{V_{FCC}}\times\left(1-f_{M_6C}-f_{M_{23}C_6}\right)+\frac{n^C_{M_6C}}{V_{M_6C}}\times f_{M_6C}+\frac{n^C_{M_{23}C_6}}{V_{M_{23}C_6}}\times f_{M_{23}C_6}\right\}:$$

$$\left\{\frac{n^M_{FCC}}{V_{FCC}}\times\left(1-f_{M_6C}-f_{M_{23}C_6}\right)+\frac{n^M_{M_6C}}{V_{M_6C}}\times f_{M_6C}+\frac{n^M_{M_{23}C_6}}{V_{M_{23}C_6}}\times f_{M_{23}C_6}\right\}=1:99, \quad (3)$$

where n_i^C is the number of C atoms in a lattice of phase i, n_i^M is the number of metallic atoms in a lattice of phase i, V_i is the unit volume of phase i, and f_i is the volume fraction of phase i. Table S1 (in the supplementary material) provides the values used to calculate the n^C_{FCC}, and please refer to Appendix A for a detailed explanation of the validity of Eq. (3). The C content in the FCC matrix (x_i^C) was obtained using the calculated n^C_{FCC} value, as follows:

$$x_i^C=\frac{n^C_{FCC}}{n^C_{FCC}+n^M_{FCC}}. \quad (4)$$

The resulting x^C_{FCC} for A800 and A900 are 0.0005 and 0.0036, respectively.

To cross-validate the C concentration we obtained, a comparison

with thermodynamic calculations were performed, using Thermo-Calc software with the TCFE2000 thermodynamic database and its upgraded version [29-32]. The FCC matrix compositions for A800 and A900 were calculated based on phase fractions from the equilibrium phase diagram (Fig. S3 in the supplementary material), and results show that calculated C concentrations closely match those obtained through Eq. (3), with particularly good agreement observed in A800, enhancing the reliability of the C concentrations we obtained. In A900, the experimentally measured C concentration is higher than the calculated value, which may be attributed either to discrepancies between the thermodynamic calculations and the experiments, or to the short heat treatment time of 10 min, which prevented the alloy from reaching equilibrium and resulted in a supersaturated FCC matrix. The observed difference in lattice parameters between A800 and A900 closely matches the difference predicted based on the C concentration variation we obtained (please see Appendix B in the supplementary material), which further validates the reliability of our determined C concentrations.

3.2. Tensile properties

Fig. 4 and S4 (in the supplementary material) depict the tensile properties of A800 and A900. A900 exhibits superior uniform and total elongations of 49.7 ± 2.2 % and 63.8 ± 2.7 %, respectively, compared to A800, which shows 46.1 ± 1.3 % and 56.0 ± 2.5 %. Despite this enhanced ductility, A900 still retains a high strength level equivalent to that of A800. Given the typical trade-off between strength and ductility, where improvements in ductility often result in the reduction of strength, this result suggests that it A900 possesses a more effective strain-hardening behavior than A800. Strain-hardening rate (SHR) curves versus true strain (ε_t) of both alloys are illustrated in Fig. 4(b). Both alloys show multi-stage strain-hardening behaviors. The strain-hardening behavior of A800 consists of a gradual decrease (stage I), followed by an increase (stage II), and a subsequent decrease in SHR (stage III), whereas that of A900 consists of a gradual decrease (stage I) followed by a plateau in SHR (stage II). During stage I, the rate of SHR decrease in A900 is less steep than that in A800, indicating that A900 shows higher SHR in the early stages of plastic deformation. However, A800 shows an earlier onset of stage II (ε_t ~0.16) compared to A900 (ε_t ~0.28), and its SHR increases rapidly, enabling it to temporarily surpass the SHR of A900. Following this rapid increase during stage II, the SHR of A800 subsequently decreases and falls below that of A900 again (stage III). By contrast, A900 exhibits a delayed onset of stage II, with its SHR curve showing a plateau rather than an increase. This plateau in SHR allows A900 to postpone necking, as determined by the Considère criterion, resulting in higher ductility compared to A800.

3.3. Deformed microstructure

The deformed microstructures of the alloys were explored through EBSD analysis (Fig. 5). The local strain (ε_{loc}) was measured using the DIC technique [33] (Supplementary Fig. S5). At a ε_{loc} of ~10 %, both alloys exhibit an almost fully FCC phase. Compared to the initial undeformed microstructure (Fig. 1(e) and (f)), the increased twin boundary fraction implies the activation of deformation twinning, with A800 and A900 showing a similar increase in twin boundary fraction. As ε_{loc} increases to ~20 %, the deformation-induced BCC martensite begins to emerge in both A800 and A900, with A800 exhibiting a higher BCC phase fraction (~1.8 %) compared to the negligible BCC phase fraction in A900 (~0.3 %). When ε_{loc} further increases to ~30 %, the BCC phase fraction of A800 sharply rises to ~13.5 %, while that of A900 remains at ~3.8 %. As the fraction of the BCC phase increases, the FCC/BCC phase boundary fraction also increases, while the twin boundary fraction decreases in both samples, implying that twin boundaries serve as nucleation sites for DIMT [11]. HCP phase was not detected in any of the EBSD analyses.

Noting that the initiation and subsequent facilitation of DIMT show similar trends to the onset of stage II in both alloys, it can be inferred that DIMT drives the change in strain-hardening behavior [12]. The newly-born BCC phase can enhance strain-hardening behavior by bearing a significant amount of applied load or generating geometrically necessary dislocations (GNDs) at the phase boundaries, a phenomenon known as the TRIP effect [7,34]. This TRIP effect accounts for the transition in strain-hardening behavior from stage I to stage II. However, since the EBSD analyses were conducted on a few localized points, it is challenging to ascertain the global DIMT kinetics, characterized by a critical strain or transformation rate; this limitation is addressed in the following in-situ synchrotron XRD results.

3.4. In-situ synchrotron XRD results

Fig. 6(a) and (b) display the in-situ synchrotron XRD line profiles of A800 and A900, each obtained at different stress/strain levels during the tensile test (Supplementary Fig. S6). During the initial stages of deformation, only the FCC peaks are observed; however, the BCC peaks emerge during plastic deformation in both alloys due to DIMT. No HCP peaks were observed across all deformation stages (Supplementary Fig. S7), indicating that a direct martensitic transformation occurred from FCC to BCC [15]. Note that such direct FCC to BCC martensitic transformation can occur through two shear deformations, as described by the Bogers-Burgers model [35]. As plastic deformation progresses, the intensity of the FCC peak decreases, while the intensity of the BCC peak increases. For A800, the intensity of the (110) BCC peak even

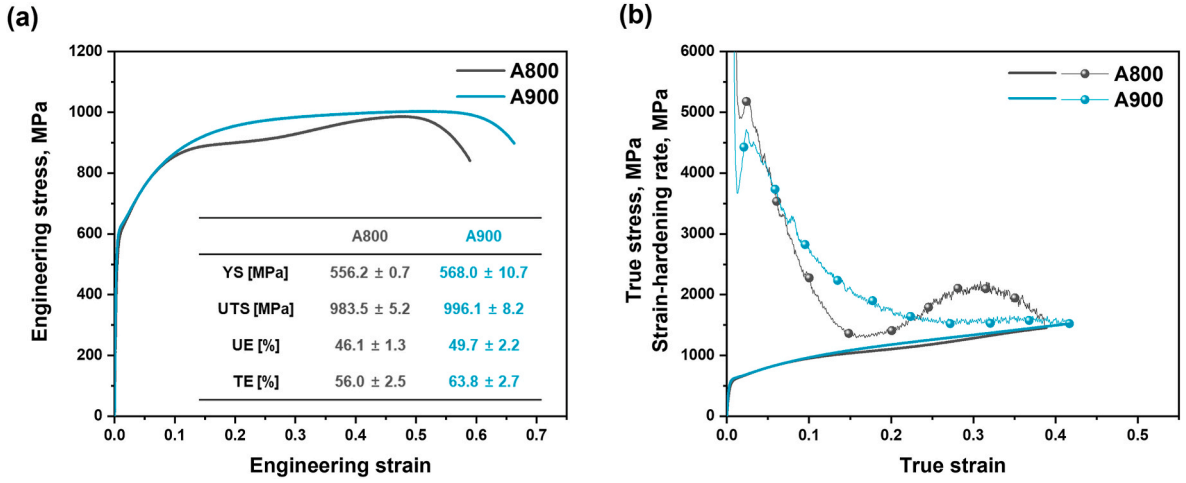

Fig. 4. (a) Engineering stress-strain curves of A800 and A900, with an inset table summarizing their tensile properties. (b) True stress-strain and strain-hardening rate curves of A800 and A900.

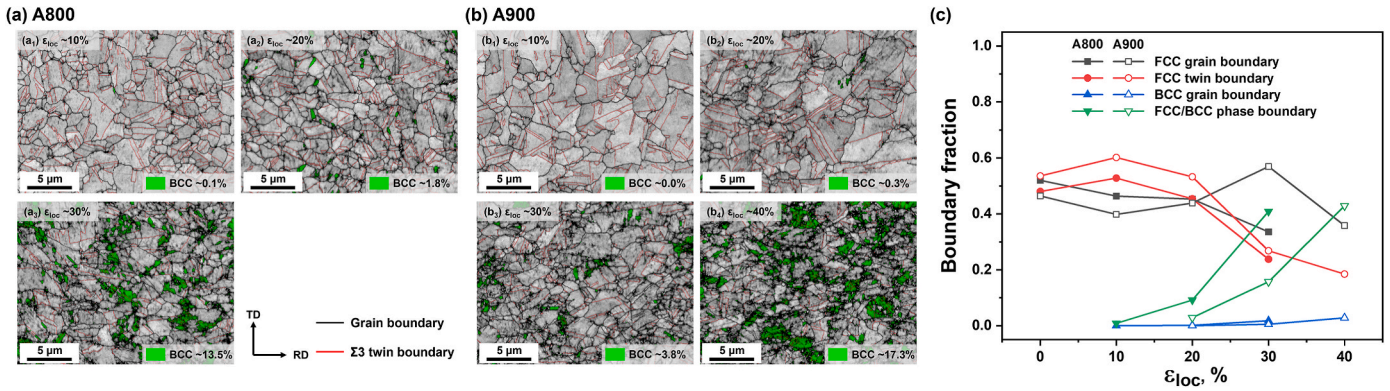

Fig. 5. EBSD IQ + BCC phase maps of tensile deformed (a) A800 and (b) A900. (c) Evolution of FCC grain boundary, FCC twin boundary, BCC grain boundary, and FCC/BCC phase boundary fractions in A800 and A900 as a function of ε_{loc}.

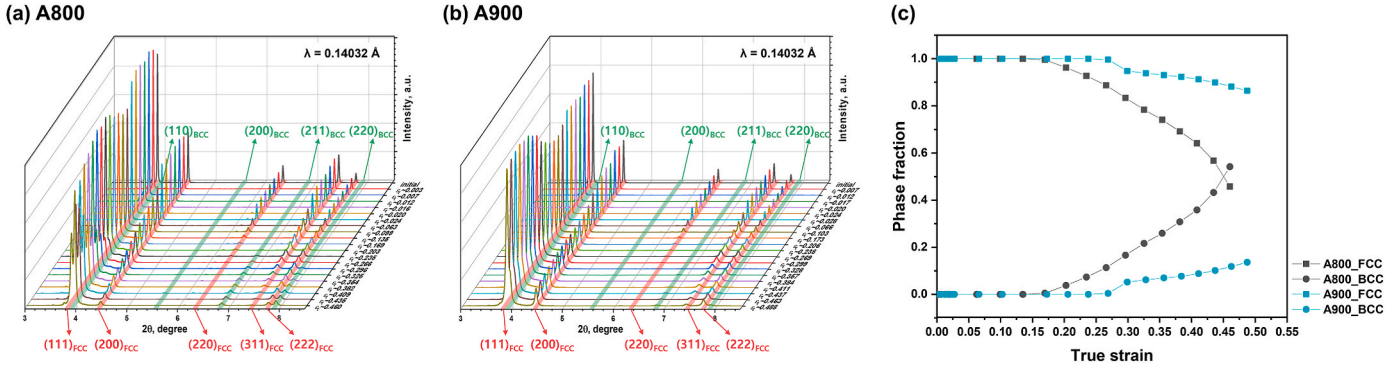

Fig. 6. In-situ synchrotron XRD patterns of (a) A800 and (b) A900 during tensile deformation. (c) Evolution of phase fractions (FCC and BCC) as a function of true strain in A800 and A900.

surpasses that of the (111) FCC peak in the later stages of deformation. In contrast, for A900, the FCC peaks remain the major peaks with higher intensity compared to the BCC peaks until the later stages of deformation. The fraction of the BCC phase can be calculated by comparing the intensities of the FCC (I^{hkl}_{FCC}) and BCC (I^{hkl}_{BCC}) peaks, as follows [36,37]:

$$f_{BCC} = \frac{\frac{1}{m}\sum_0^m I^{hkl}_{BCC} \Big/ R^{hkl}_{BCC}}{\frac{1}{n}\sum_0^n I^{hkl}_{FCC} \Big/ R^{hkl}_{FCC} + \frac{1}{m}\sum_0^m I^{hkl}_{BCC} \Big/ R^{hkl}_{BCC}}, \tag{5}$$

where R^{hkl}_i is the theoretically calculated peak intensity of the hkl planes in phase i, and $n = 5$ and $m = 4$ represent the numbers of diffraction peaks for the FCC and BCC phases, respectively. The calculated phase fraction evolutions of A800 and A900 are comparatively shown in Fig. 6 (c). A800 shows an earlier activation of DIMT compared to A900; the critical strains for DIMT in A800 and A900 are ~0.17 and ~0.23, respectively. Additionally, A800 exhibits a significantly accelerated transformation rate compared to A900. Taken together, these results confirm that A800 demonstrates faster DIMT kinetics than A900.

Another notable feature in the in-situ synchrotron XRD line profiles is the leftward shift of the peaks, indicating an increase in lattice spacing. By tracing the increase in lattice spacing of the FCC phase (d^{hkl}_{FCC}), the lattice strain of a hkl plane of the FCC phase (ε^{hkl}_{FCC}) can be calculated, as follows:

$$\varepsilon^{hkl}_{FCC} = \frac{d^{hkl}_{FCC} - d^{hkl}_{FCC,0}}{d^{hkl}_{FCC,0}}, \tag{6}$$

where $d^{hkl}_{FCC,0}$ is the initial lattice spacing obtained from Fig. 1(a). The calculated evolution of lattice strain for the FCC phase in A800 and A900 is depicted in Fig. 7(a) through 7(d). In both alloys, the lattice strains of all hkl planes exhibit linear responses to applied true stress/strain during the elastic deformation stages but begin to display non-linear responses after yielding. By performing a linear fitting of the lattice strain response versus applied true stress during the elastic deformation (Fig. 7(c) and (d)), the elastic moduli of each FCC plane (E^{hkl}_{FCC}) can be obtained, and the results are summarized in Table 3. Meanwhile, a clear separation in lattice strain is observed among the FCC planes. The (200) grain family exhibits the highest lattice strain, while the (111) and (220) grain families show relatively low lattice strains. This variation in lattice strain within the FCC grain families arises due to orientation-dependent plasticity [38,39].

The FCC phase stress (σ_{FCC}) can be determined using the following equation [36]:

$$\sigma_{FCC} = \sum_0^n \frac{I^{hkl}_{FCC}/R^{hkl}_{FCC}}{\sum_0^n I^{hkl}_{FCC}/R^{hkl}_{FCC}} \cdot E^{hkl}_{FCC} \cdot \varepsilon^{hkl}_{FCC}. \tag{7}$$

By comparing the FCC phase stresses of A800 and A900, it is observed that A900 exhibits higher FCC phase stress throughout the entire plastic deformation compared to A800 (Fig. 7(e)). Additionally, SHR curves from the derivative of the FCC phase stresses reveal that the FCC phase in A900 demonstrates a higher SHR than that in A800 (Fig. 7 (f)).

4. Discussion

4.1. Strengthening mechanism

The yield strength (σ_{YS}) of A800 and A900 can be estimated using the

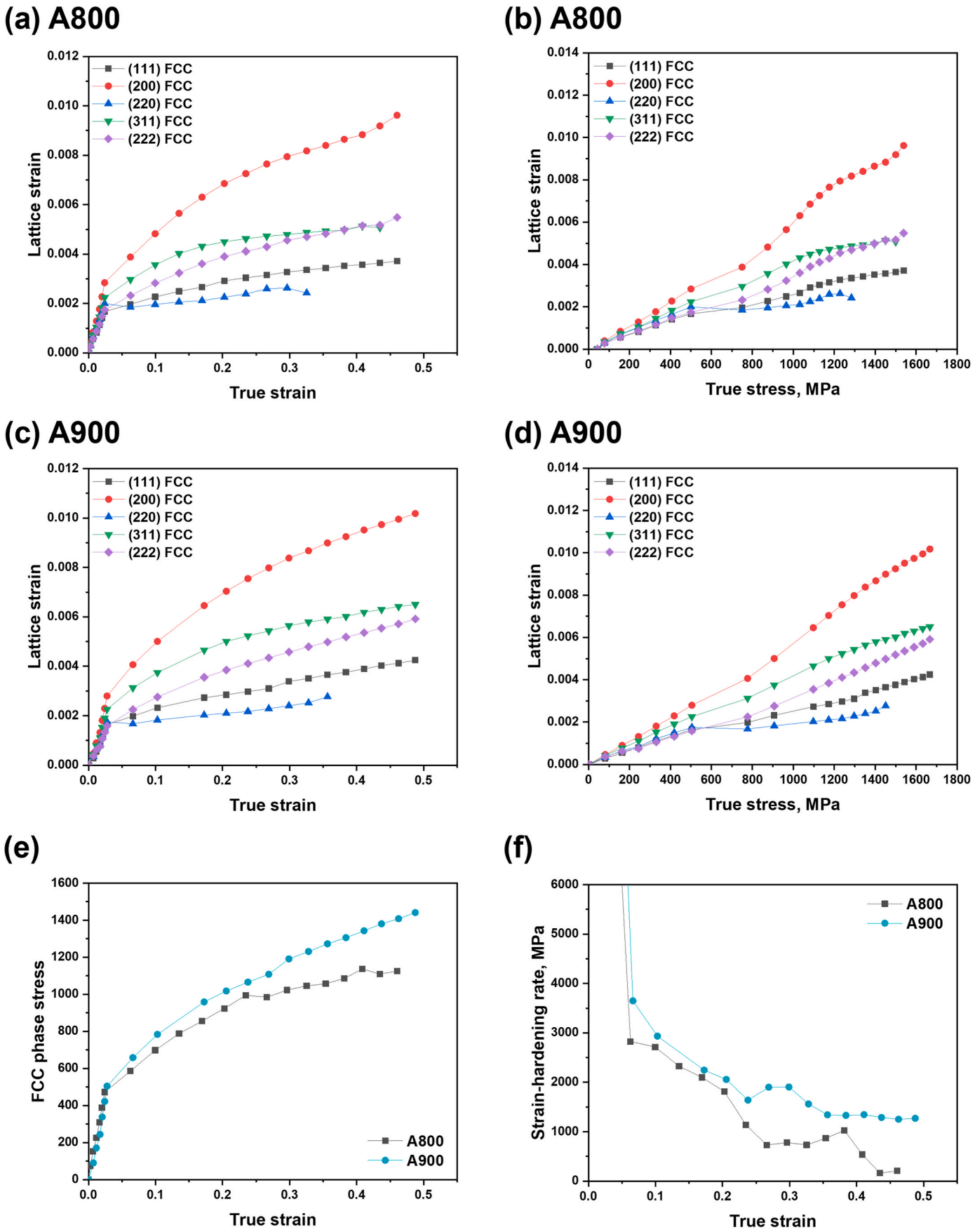

Fig. 7. (a, b) Lattice strain evolution of A800 versus (a) true strain and (b) true stress. (c, d) Lattice strain evolution of A900 versus (c) true strain and (d) true stress. (e) Evolution of the FCC phase stress and the corresponding strain-hardening rate curves of A800 and A900.

Table 3
E_{FCC}^{hkl} of A800 and A900.

	$E_{FCC}^{(111)}$ [GPa]	$E_{FCC}^{(200)}$ [GPa]	$E_{FCC}^{(220)}$ [GPa]	$E_{FCC}^{(311)}$ [GPa]	$E_{FCC}^{(222)}$ [GPa]
A800	281.8	166.8	234.2	211.3	268.0
A900	305.6	181.3	288.9	224.3	328.6

following equation [10]:

$$\sigma_{YS} = \sigma_0 + \Delta\sigma_{gb} + \Delta\sigma_{ppt} + \Delta\sigma_{ss}, \tag{8}$$

where σ_0, $\Delta\sigma_{gb}$, $\Delta\sigma_{ppt}$, and $\Delta\sigma_{ss}$ represent the lattice friction stress, grain boundary strengthening, precipitation strengthening, and solid solution strengthening, respectively.

The grain boundary strengthening can be described by the Hall-Petch relation as follows [40]:

$$\Delta\sigma_{gb} = K_y \cdot D^{-0.5}, \tag{9}$$

where K_y is the Hall-Petch coefficient and D is the average grain size. Given that abundant annealing twin boundaries in A800 and A900 also serve as effective barriers to dislocation glide, the Hall-Petch relation can be modified as follows [41,42]:

$$\Delta\sigma_{gb} = K_y \cdot {D_{eff}}^{-0.5}, \tag{10}$$

$$D_{eff} = \frac{D}{1 + k\ln(D/D_0)}, \tag{11}$$

where D_{eff} is the effective grain size considering annealing twin boundaries, D_0 the smallest grain size containing annealing twin, and k = 0.4 [41] the constant. Using D_0 = ~0.95 μm for A800 and D_0 = ~0.78 μm for A900, the average grain sizes were converted to effective grain sizes of ~1.73 μm for A800 and ~1.72 μm for A900. Since A800 and A900 have similar effective grain sizes, their calculated $\Delta\sigma_{gb}$ values, by taking K_y = 494 MPa $\mu m^{0.5}$ from the CoCrFeMnNi HEA [43], are also close, at ~375.6 MPa and ~376.7 MPa, respectively.

In the case of precipitation strengthening, two types of carbides, M_6C and $M_{23}C_6$, contribute through the Orowan mechanism due to their non-shearable nature [10,44,45]. The Orowan mechanism is expressed as follows [14,46]:

$$\Delta\sigma_{ppt} = 0.538\frac{Gbf^{0.5}\ln\frac{d}{b}}{d}, \tag{12}$$

$$d = \left(\frac{3}{2}\right)^{0.5} \cdot d_0, \tag{13}$$

where G, b, f, d, and d_0 represent the shear modulus (~82.3 GPa borrowed from Ref. [7]), the magnitude of the Burgers vector (~0.2531 nm for A800 and ~0.2534 nm for A900), the volume fraction of the carbides, the real spatial diameter of the carbides, and the average diameter of the carbides, respectively. The $\Delta\sigma_{ppt}$ values of A800 and A900 were calculated as ~52.8 MPa and ~44.6 MPa, respectively. It should be noted that A900 exhibits precipitation strengthening comparable to A800, despite having a ~32 % lower carbide volume fraction. Given that A900 has a smaller average radius, this is due to the characteristics of the Orowan mechanism, where a smaller precipitate size leads to a greater strengthening effect.

Attention is now shifted to solid solution strengthening. In the Co-Cr-Fe-Ni-Mo-C FeMEA, Mo and C contribute to solid solution strengthening [10]. Mo atoms, having a large atomic radius, serve as substitutional atoms and amplify lattice distortion [47,48], whereas C atoms occupy interstitial sites in the FCC matrix and generate interstitial strengthening [49]. Therefore, Mo and C atoms alloyed in the FCC matrix increase resistance to dislocation glide, and the resulting increase in friction stress can be expressed as $\sigma_0 + \Delta\sigma_{ss}$. It is revealed by the STEM analysis (section 3.1) that the FCC matrix in A900 contains more Mo and C content (Mo = ~2.71 at% and C = ~0.36 at%) than in A800 (Mo = ~2.10 at% and C = ~0.05 at%). Using the solid solution strengthening values of ~78 MPa/at% from the C-doped CoCrFeMnNi HEA [49] and ~2.4 MPa/at% from the Mo-doped CoCrFeMnNi HEA [47], along with the lattice friction stress value of ~125 MPa from the CoCrFeMnNi HEA [43], the $\sigma_0 + \Delta\sigma_{ss}$ values were calculated to be ~133.9 MPa for A800 and ~159.5 MPa for A900.

The stacked contributions of each strengthening mechanism are depicted in Fig. 8. The calculated yield strengths of both alloys are well matched with the experimental yield strengths ($\sigma_{YS,exp}$). It can be observed that as precipitation strengthening intensifies, solid solution strengthening weakens, indicating that precipitation and lattice distortion compete in contributing to the strengthening mechanisms. By comparing the strengthening mechanisms of both alloys, the reason A900 exhibits yield strength as high as that of A800, despite having a lower carbide volume fraction, can be summarized as follows; A900 benefits from its smaller carbide size, which contributes to effective precipitation strengthening, while the higher Mo and C content in the FCC matrix significantly enhances solid solution strengthening.

4.2. Deformation mechanism

During the early stages of plastic deformation, A900 shows a higher SHR than A800. In-situ synchrotron XRD analysis (section 3.4) reveals that the FCC matrix in A900 experiences higher phase stress and SHR than that in A800, implying that the intrinsically higher strain-hardenability of the FCC phase in A900 is responsible for its enhanced SHR in the early stages of deformation. To further elucidate the underlying mechanism, the back stress (σ_{back}) and effective stress (σ_{eff}) are evaluated by LUR tests using the following equations [50]:

$$\sigma_{eff} = \frac{A_{loop}}{2w_{loop}}, \tag{14}$$

$$\sigma_{back} = \sigma_{flow} - \sigma_{eff}, \tag{15}$$

where A_{loop} and w_{loop} represent the area and width of each hysteresis loop, respectively, and σ_{flow} is the flow stress. In Fig. 9(c), the calculated σ_{back} and σ_{eff} for each specimen reveal that A900 exhibits a steeper increase in back stress compared to A800, with a more pronounced back stress contribution. This suggests that the superior strain-hardenability of the FCC phase in A900 is primarily attributed to enhanced back stress.

Back stress originates from the long-range interactions of dislocations accumulated at microstructural obstacles such as grain boundaries, twin boundaries, and coarse precipitates [51]. The enhanced back stress

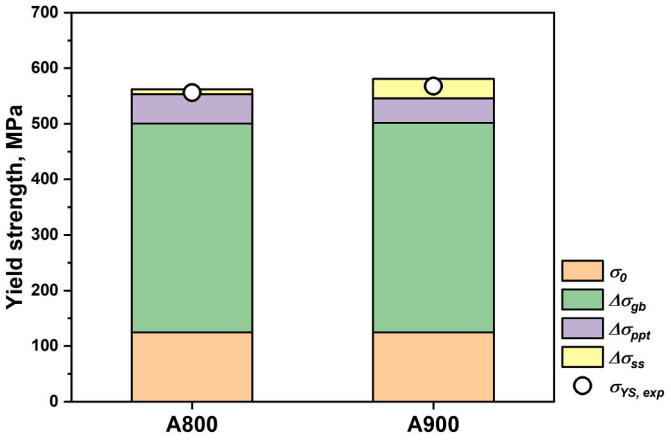

Fig. 8. The calculated contributions of each strengthening mechanism in A800 and A900. The stacked heights represent the calculated yield strengths, with the experimental yield strengths presented for comparison.

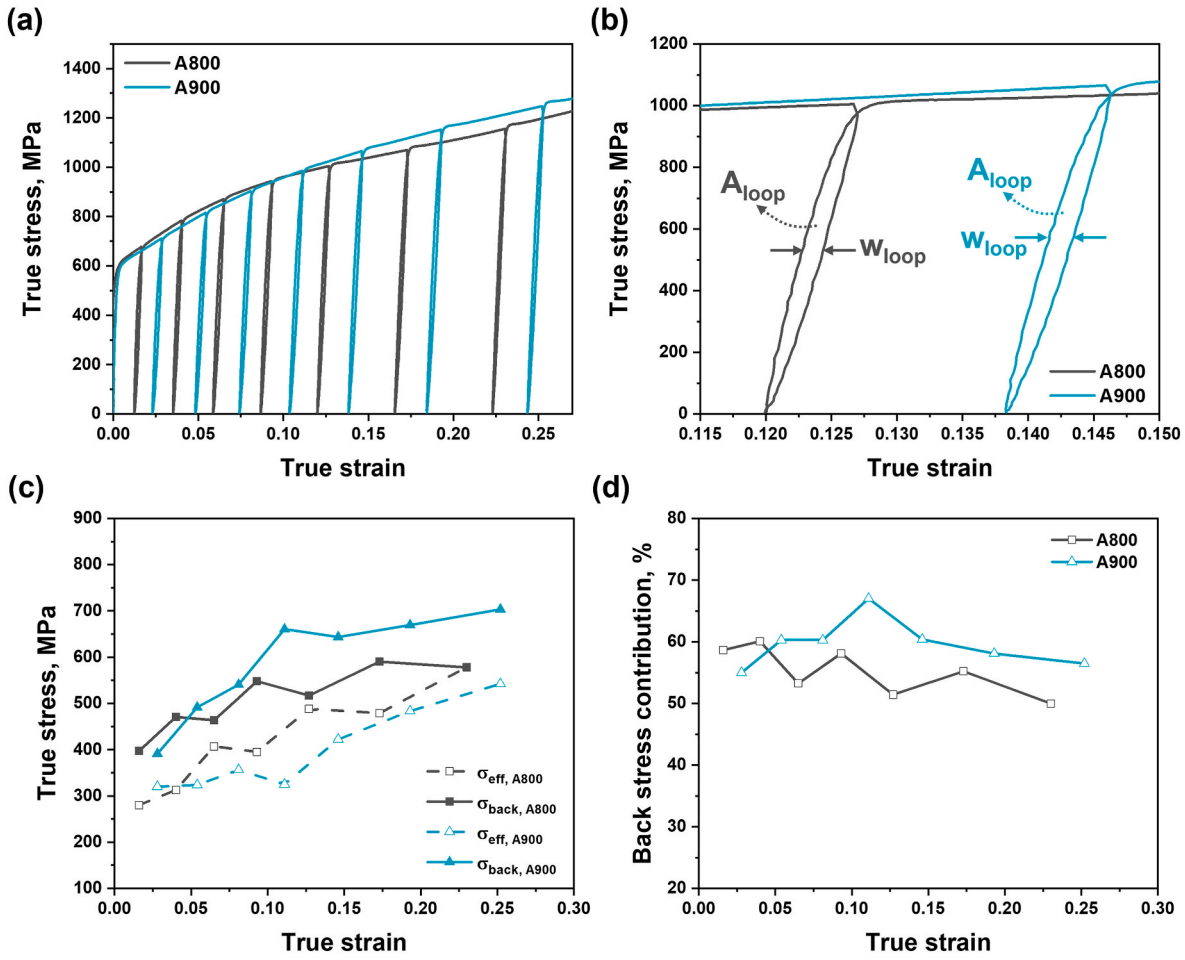

Fig. 9. (a) LUR stress-strain curves and (b) an enlarged view of the 5th hysteresis loops for A800 and A900. Evolution of (c) back stress and effective stress, and (d) back stress contribution.

observed in A900 suggests more effective dislocation pile-up in A900 compared to A800 during the early stages of plastic deformation, where the density of boundaries newly generated by deformation twins is comparable (Fig. 5(c)). FCC-structured HEAs or MEAs are known to exhibit strong slip planarity due to severe lattice distortion, which promotes effective dislocation pile-up at boundaries and leads to high back stress, a phenomenon known as lattice distortion-induced back stress [20,21,24]. Severe lattice distortion in HEAs and MEAs significantly impedes the recombination of separated partial dislocations, which is essential for cross slip [52], thereby enhancing slip planarity and contributing to high back stress. A800 and A900 also exhibit strong slip planarity, as confirmed by post-mortem ECCI analysis (Supplementary Fig. S8), with A900 showing a higher slip planarity, while A800 displays more tangled dislocations deviating from slip planes. Notably, the FCC matrix in A900 contains higher concentrations of solute Mo and C atoms, resulting in greater lattice distortion compared to A800. Consequently, the FCC matrix in A900 exhibits more significant lattice distortion-mediated back stress than that of A800, which primarily accounts for the superior back stress. Please note that although A800 contains a higher fraction of coarse precipitates, which can serve as dislocation obstacles, the overall back stress is higher in A900. Previous studies investigating the impact of Mo or C additions on the mechanical properties of HEAs have reported a similar tendency of increasing SHR with greater lattice distortion [18,19,53], which strongly supports our finding. In addition, the earlier activation and accelerated transformation rate of DIMT in A800 may also contribute to SHR degradation by accommodating global strain through transformation plasticity, resulting in a stress-relaxation effect [54,55].

As plastic deformation advances, DIMT occurs rapidly, and the newly formed hard BCC martensite generates a strengthening effect based on the rule of mixtures [23,36,54]. Consequently, A800, which exhibits faster DIMT kinetics, enters stage II earlier than A900. Grain size is generally known as a vital factor influencing DIMT kinetics [36,56]; however, since the average grain size and grain size distribution of A800 and A900 are similar, the grain size effect can be ruled out in this case. To investigate the reason behind the different DIMT kinetics between A800 and A900, the Gibbs free energy differences between the FCC and BCC phases ($\Delta G^{FCC\rightarrow BCC}$) were calculated based on the experimentally obtained matrix compositions of A800 and A900 (Table 2). The calculated $\Delta G^{FCC\rightarrow BCC}$ of A800 is lower than that of A900 (Fig. 10), suggesting that the phase stability of the FCC matrix in A800 is lower than that in A900, which provides a higher driving force for DIMT. The reduced phase stability of the FCC matrix in A800 arises from changes in the matrix composition due to precipitation, a phenomenon known as precipitation-driven metastability [10]. The present calculation result is in accordance with previous works on the Co-Cr-Fe-Ni-Mo-C FeMEA system, where active carbide precipitation decreased the FCC phase stability [10,12]. Therefore, the more extensive carbide precipitation in A800 than A900 leads to faster DIMT kinetics. Additionally, the higher precipitate volume fraction in A800 is more advantageous for the initiation of DIMT than in A900, as stress concentrations around the precipitates can promote DIMT [12].

Following the hump in SHR, A800 experiences a decline in SHR, caused by the initiation of plastic deformation in the newly formed BCC phase [57,58]. As a result, the SHR falls below that of A900 again, and A800 quickly enters necking. Meanwhile, A900 exhibits a delayed

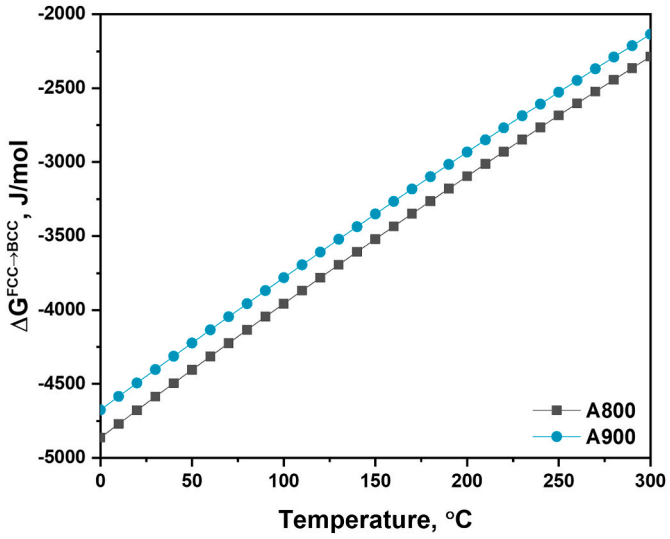

Fig. 10. Calculated $\Delta G^{FCC \rightarrow BCC}$ of A800 and A900 as a function of temperature.

activation of DIMT and a later entrance into stage II. Attributed to the DIMT-mediated TRIP effect, the SHR remains steady instead of decreasing, which delays necking and consequently enhances ductility.

To summarize the deformation mechanisms, while greater lattice distortion amplifies back stress in A900, prompted precipitation facilitates DIMT kinetics and enhances the SHR in A800, highlighting the competitive interaction between lattice distortion and precipitation in influencing the deformation mechanisms. It is important to note that although A800 temporarily exhibits higher SHR than A900 due to more active DIMT, the superior strain-hardenability of the FCC matrix in A900, which contains more Mo and C atoms, leads to higher strain-hardening in the early stages of plastic deformation, ultimately resulting in a high UTS for A900, comparable to that of A800. In addition, delayed DIMT in A900 results in the postponed necking and an increase in ductility. Therefore, it can be concluded that by suppressing precipitation and enhancing the degree of lattice distortion, utilizing lattice distortion-induced back stress as the primary strain-hardening mechanism, while employing delayed DIMT as the ductilizing mechanism, enhanced tensile properties were achieved.

5. Conclusions

This study demonstrates a strategy to improve tensile properties in $Co_{18}Cr_{13}Fe_{57.5}Ni_{7.5}Mo_3C_1$ FeMEA by leveraging the competitive interplay between precipitation and lattice distortion in the strengthening and deformation mechanisms. By altering the annealing conditions, the precipitation of M_6C and $M_{23}C_6$ carbides was suppressed in A900 (annealed at 900 °C for 10 min), leading to lower area fractions and finer precipitate sizes compared to A800 (annealed at 800°C for 3 h), without changing the average grain size. The changes in precipitation alter the degree of lattice distortion, which is harnessed to tune both the strengthening and deformation mechanisms, resulting in A900 demonstrating enhanced tensile properties compared to A800. The reasons why the A900 maintains a yield strength as high as that of A800, despite its lower carbide fraction, are as follows: (i) refining carbide size to minimize the reduction in precipitation strengthening, and (ii) enhancing lattice distortion and solid solution strengthening by increasing the solute concentrations of Mo and C in the FCC matrix. Additionally, the balanced utilization of the lattice distortion-induced back stress and DIMT enhances strain-hardenability, leading to superior ductility without sacrificing strength. By incorporating more solute Mo and C atoms in the FCC matrix, both lattice friction and phase stability of the FCC matrix are increased. Consequently, improved lattice distortion-induced back stress enhances the strain-hardening of A900 compared to A800 in the early stages of deformation, while the delayed activation of DIMT prevents the onset of deformation localization and improves ductility. This work provides a comprehensive understanding of strengthening and deformation mechanisms in Co-Cr-Fe-Ni-Mo-C FeMEAs along with strategies to enhance their mechanical properties, which can help accelerate the practical application of these alloys. Furthermore, by offering insights into how the control of precipitation and lattice distortion can effectively enhance tensile properties, this study paves the way for improving mechanical properties in other alloys and designing new high-performance alloys using similar strategies.

CRediT authorship contribution statement

Jae Heung Lee: Writing – original draft, Visualization, Validation, Software, Methodology, Investigation, Formal analysis, Data curation, Conceptualization. **Hyeonseok Kwon:** Writing – review & editing, Validation, Supervision, Methodology, Investigation, Formal analysis, Data curation, Conceptualization. **Gang Hee Gu:** Methodology, Investigation, Formal analysis, Data curation. **Ji Yeong Lee:** Methodology, Investigation, Formal analysis, Data curation. **Sang Guk Jeong:** Methodology, Investigation, Formal analysis, Data curation. **Emad Maawad:** Methodology, Investigation, Formal analysis, Data curation. **Changwan Ha:** Validation, Methodology, Formal analysis. **Jaemin Wang:** Software, Methodology, Formal analysis, Data curation. **Byeong-Joo Lee:** Validation, Software, Methodology. **Sangbong Yi:** Supervision, Software, Project administration, Methodology, Investigation, Formal analysis, Data curation. **Takayoshi Nakano:** Validation, Methodology. **Hyoung Seop Kim:** Writing – review & editing, Validation, Supervision, Resources, Project administration, Funding acquisition.

Declaration of competing interest

The authors declare that they have no known competing financial interests or personal relationships that could have appeared to influence the work reported in this paper.

Acknowledgment

This study was financially supported by the National Research Foundation of Korea (NRF) grant funded by the Ministry of Science and ICT (RS-2023-00281246 and NRF-2022R1A5A1030054). We acknowledge DESY (Hamburg, Germany), a member of the Helmholtz Association HGF, for the provision of experimental facilities. Parts of this research were carried out at the P07 beamline, which is operated by the Helmholz-Zentrum Hereon, and we would like to thank Dr. Norbert Schell for assistance.

Appendix A. Supplementary data

Supplementary data to this article can be found online at https://doi.org/10.1016/j.msea.2025.148642.

Data availability

Data will be made available on request.

References

[1] J.W. Yeh, S.K. Chen, S.J. Lin, J.Y. Gan, T.S. Chin, T.T. Shun, C.H. Tsau, S.Y. Chang, Nanostructured high-entropy alloys with multiple principal elements: novel alloy design concepts and outcomes, Adv. Eng. Mater. 6 (2004) 299–303.
[2] B. Cantor, I. Chang, P. Knight, A. Vincent, Microstructural development in equiatomic multicomponent alloys, Mater. Sci. Eng. A 375 (2004) 213–218.
[3] E.P. George, D. Raabe, R.O. Ritchie, High-entropy alloys, Nat. Rev. Mater. 4 (2019) 515–534.
[4] Z. Li, K.G. Pradeep, Y. Deng, D. Raabe, C.C. Tasan, Metastable high-entropy dual-phase alloys overcome the strength–ductility trade-off, Nature 534 (2016) 227–230.

[5] M.S. Mehranpour, M.J. Sohrabi, A. Kalhor, J.H. Lee, A. Heydarinia, H. Mirzadeh, S. Sadeghpour, K. Rodak, M. Nili-Ahmadabadi, R. Mahmudi, Exceptional strength-ductility synergy in the novel metastable FeCoCrNiVSi high-entropy alloys via tuning the grain size dependency of the transformation-induced plasticity effect, Int. J. Plast. 182 (2024) 104115.
[6] J.W. Bae, J.B. Seol, J. Moon, S.S. Sohn, M.J. Jang, H.Y. Um, B.-J. Lee, H.S. Kim, Exceptional phase-transformation strengthening of ferrous medium-entropy alloys at cryogenic temperatures, Acta Mater. 161 (2018) 388–399.
[7] J.W. Bae, J.G. Kim, J.M. Park, W. Woo, S. Harjo, H.S. Kim, In situ neutron diffraction study of phase stress evolution in a ferrous medium-entropy alloy under low-temperature tensile loading, Scr. Mater. 165 (2019) 60–63.
[8] S. Park, H. Nam, Y. Lee, N. Park, S. Hong, Y. Na, C. Park, N. Kang, Enhancement of hardness and yield strength induced by cu-rich phase and its effect at cryogenic temperature on gas tungsten arc welds of ferrous medium-entropy alloy, Met. Mater. Int. 29 (2023) 2316–2330.
[9] J.W. Bae, H.S. Kim, Towards ferrous medium-entropy alloys with low-cost and high-performance, Scr. Mater. 186 (2020) 169–173.
[10] H. Kwon, J. Moon, J.W. Bae, J.M. Park, S. Son, H.-S. Do, B.-J. Lee, H.S. Kim, Precipitation-driven metastability engineering of carbon-doped CoCrFeNiMo medium-entropy alloys at cryogenic temperature, Scr. Mater. 188 (2020) 140–145.
[11] H. Kwon, A. Zargaran, P. Asghari-Rad, E.S. Kim, G.H. Gu, J. Lee, J. Moon, J.W. Bae, H.S. Kim, Metastability engineering of partially recrystallized C-doped non-equiatomic CoCrFeNiMo medium-entropy alloy, Appl. Phys. Lett. 119 (2021) 141901.
[12] J.Y. Lee, H. Kwon, J.H. Lee, J. Kwon, J. Wang, J.W. Bae, J. Moon, B.-J. Lee, Y.-U. Heo, H.S. Kim, Regulation of cryogenic mechanical behaviors of C-added non-equiatomic CoCrFeNiMo ferrous medium-entropy alloy via control of initial microstructure, J. Mater. Sci. Technol. 208 (2025) 141–151.
[13] J.M. Park, H. Kwon, J. Choe, K.T. Kim, J.-H. Yu, Y.-U. Heo, H.S. Kim, Cell boundary engineering of ferrous medium-entropy alloy fabricated by laser powder bed fusion, Scr. Mater. 237 (2023) 115715.
[14] H. Kwon, E.S. Kim, Y.-U. Heo, J. Choe, R.E. Kim, S.Y. Ahn, S.-H. Oh, J.M. Park, B.-J. Lee, H.S. Kim, Restructuring the cell network of non-equiatomic CoCrFeNiMoC medium-entropy alloy fabricated by laser powder bed fusion, J. Mater. Sci. Technol. 214 (2024) 143–152.
[15] J.H. Lee, H. Kwon, G.H. Gu, J.Y. Lee, S.G. Jeong, E. Maawad, C. Ha, J.B. Seol, S. I. Hong, S. Yi, Complex deformation behavior of a partially recrystallized metastable medium-entropy alloy: in-situ synchrotron X-ray diffraction study, Acta Mater. 286 (2025) 120757.
[16] H. Kwon, J.H. Lee, J.Y. Lee, G.H. Gu, S.G. Jeong, C. Ha, J. Wang, B.-J. Lee, E. Mawaad, S. Yi, Activating metastability engineering via control of initial microstructure in C-Added CoCrFeNiMo medium-entropy alloy: in situ X-Ray diffraction study, Mater. Sci. Eng. A 924 (2025) 147797.
[17] H.D. Park, J.W. Won, J. Moon, H.S. Kim, H. Sung, J.B. Seol, J.W. Bae, J.G. Kim, Fe55Co17. 5Ni10Cr12. 5Mo5 high-entropy alloy with outstanding cryogenic mechanical properties driven by deformation-induced phase transformation behavior, Met. Mater. Int. 29 (2023) 95–107.
[18] J. Li, K. Yamanaka, A. Chiba, Significant lattice-distortion effect on compressive deformation in Mo-added CoCrFeNi-based high-entropy alloys, Mater. Sci. Eng. A 830 (2022) 142295.
[19] Z. Wang, I. Baker, W. Guo, J.D. Poplawsky, The effect of carbon on the microstructures, mechanical properties, and deformation mechanisms of thermo-mechanically treated Fe40. 4Ni11. 3Mn34. 8Al7. 5Cr6 high entropy alloys, Acta Mater. 126 (2017) 346–360.
[20] O. Bouaziz, J. Moon, H.S. Kim, Y. Estrin, Isotropic and kinematic hardening of a high entropy alloy, Scr. Mater. 191 (2021) 107–110.
[21] Y. Kim, P. Asghari-Rad, J. Lee, G.H. Gu, M. Jang, O. Bouaziz, Y. Estrin, H. Kato, H. S. Kim, Solid solution induced back-stress in multi-principal element alloys: experiment and modeling, Mater. Sci. Eng. A 835 (2022) 142621.
[22] J. Shen, J. Lopes, Z. Zeng, Y.T. Choi, E. Maawad, N. Schell, H.S. Kim, R.S. Mishra, J. Oliveira, Deformation behavior and strengthening effects of an eutectic AlCoCrFeNi2. 1 high entropy alloy probed by in-situ synchrotron X-ray diffraction and post-mortem EBSD, Mater. Sci. Eng. A 872 (2023) 144946.
[23] H. Kwon, S. Harjo, T. Kawasaki, W. Gong, S.G. Jeong, E.S. Kim, P. Sathiyamoorthi, H. Kato, H.S. Kim, Work hardening behavior of hot-rolled metastable Fe50Co25Ni10Al5Ti5Mo5 medium-entropy alloy: in situ neutron diffraction analysis, Sci. Technol. Adv. Mater. 23 (2022) 579–586.
[24] J.M. Park, D.C. Yang, H.-J. Kim, D.G. Kim, S. Lee, H.S. Kim, S.S. Sohn, Ultra-strong and strain-hardenable ultrafine-grained medium-entropy alloy via enhanced grain-boundary strengthening, Mater. Res. Lett. 9 (2021) 315–321.
[25] J. Lee, S.I. Hong, S.-H. Joo, H.S. Kim, Insights into strain delocalization and plasticity in pre-deformed metastable dual-phase medium-entropy alloys, Mater. Sci. Eng. A 937 (2025) 148445.
[26] P. Muhammed Shafi, A. Chandra Bose, Impact of crystalline defects and size on X-ray line broadening: a phenomenological approach for tetragonal SnO2 nanocrystals, AIP Adv. 5 (2015).
[27] D.A. Porter, K.E. Easterling, Phase Transformations in Metals and Alloys, CRC press, Florida, 2009.
[28] L. Wang, C. Gu, C. Zhang, Z. Feng, J. Yi, Hierarchical Cu-Rich nanoprecipitates in a CoFeTiVCu high-entropy alloy and its impressed strength-plasticity balance, Met. Mater. Int. 29 (2023) 1951–1960.
[29] J.-O. Andersson, T. Helander, L. Höglund, P. Shi, B. Sundman, Thermo-Calc & DICTRA, computational tools for materials science, Calphad 26 (2002) 273–312.
[30] W.-M. Choi, Y.H. Jo, D.G. Kim, S.S. Sohn, S. Lee, B.-J. Lee, A thermodynamic description of the Co-Cr-Fe-Ni-V system for high-entropy alloy design, Calphad 66 (2019) 101624.
[31] H.-S. Do, T.J. Jang, K.J. Kim, S.S. Sohn, B.-J. Lee, A novel high-entropy alloy with multi-strengthening mechanisms: activation of TRIP effect in C-doped high-entropy alloy, Mater. Sci. Eng. A 859 (2022) 144220.
[32] B. Sundman, TCFE2000: the Thermo-Calc Steels Database, Upgraded by B.-J. Lee, KTH, Stockholm, 1999.
[33] G.H. Gu, Y. Kim, R.E. Kim, M.H. Seo, H.S. Kim, A new digital image correlation method for measuring wide strain range true stress–strain curve of clad materials, Met. Mater. Int. 29 (2023) 168–173.
[34] B. De Cooman, Structure–properties relationship in TRIP steels containing carbide-free bainite, Curr. Opin. Solid State Mater. Sci. 8 (2004) 285–303.
[35] T. Shimokawa, K. Fujii, T. Niiyama, Atomic simulation study of the factors affecting nucleation in deformation-induced martensitic transformation in grains and at grain boundaries in pure iron, Acta Mater. 265 (2024) 119629.
[36] W. Mao, W. Gong, S. Harjo, S. Morooka, S. Gao, T. Kawasaki, N. Tsuji, In situ neutron diffraction revealing the achievement of excellent combination of strength and ductility in metastable austenitic steel by grain refinement, J. Mater. Sci. Technol. 176 (2024) 69–82.
[37] M.J. Sohrabi, M.S. Mehranpour, J.H. Lee, A. Heydarinia, H. Mirzadeh, H.S. Kim, Overcoming strength-ductility trade-off in Si-containing transformation-induced plasticity high-entropy alloys via metastability engineering, Mater. Sci. Eng. A 908 (2024) 146766.
[38] Y. Tomota, P. Lukas, S. Harjo, J. Park, N. Tsuchida, D. Neov, In situ neutron diffraction study of IF and ultra low carbon steels upon tensile deformation, Acta Mater. 51 (2003) 819–830.
[39] B. Clausen, T. Lorentzen, T. Leffers, Self-consistent modelling of the plastic deformation of fcc polycrystals and its implications for diffraction measurements of internal stresses, Acta Mater. 46 (1998) 3087–3098.
[40] J.H. Lee, H. Kwon, P. Sathiyamoorthi, S. Son, H.S. Kim, Synergic combination of strength and ductility through both grain refinement and precipitation in Al0. 3CoCrNi medium-entropy alloy, Adv. Eng. Mater. 25 (2023) 2201930.
[41] C.S. Pande, B. Rath, M. Imam, Effect of annealing twins on Hall–Petch relation in polycrystalline materials, Mater. Sci. Eng. A 367 (2004) 171–175.
[42] M. Rezayat, F. Najib, Grain refinement of CoNiCrMo non-equiatomic medium entropy alloy, Met. Mater. Int. 29 (2023) 235–246.
[43] F. Otto, A. Dlouhý, C. Somsen, H. Bei, G. Eggeler, E.P. George, The influences of temperature and microstructure on the tensile properties of a CoCrFeMnNi high-entropy alloy, Acta Mater. 61 (2013) 5743–5755.
[44] D. Errandonea, J. Ruiz-Fuertes, J. Sans, D. Santamaría-Perez, O. Gomis, A. Gómez, F. Sapiña, Compressibility and structural stability of ultra-incompressible bimetallic interstitial carbides and nitrides, Phys. Rev. B Condens. Matter 85 (2012) 144103.
[45] J. Li, B. Gao, Y. Wang, X. Chen, Y. Xin, S. Tang, B. Liu, Y. Liu, M. Song, Microstructures and mechanical properties of nano carbides reinforced CoCrFeMnNi high entropy alloys, J. Alloys Compd. 792 (2019) 170–179.
[46] T. Gladman, Precipitation hardening in metals, Mater. Sci. Technol. 15 (1999) 30–36.
[47] G. Qin, R. Chen, H. Zheng, H. Fang, L. Wang, Y. Su, J. Guo, H. Fu, Strengthening FCC-CoCrFeMnNi high entropy alloys by Mo addition, J. Mater. Sci. Technol. 35 (2019) 578–583.
[48] W. Liu, Z. Lu, J. He, J. Luan, Z. Wang, B. Liu, Y. Liu, M. Chen, C. Liu, Ductile CoCrFeNiMox high entropy alloys strengthened by hard intermetallic phases, Acta Mater. 116 (2016) 332–342.
[49] J.M. Park, J. Choe, J.G. Kim, J.W. Bae, J. Moon, S. Yang, K.T. Kim, J.-H. Yu, H. S. Kim, Superior tensile properties of 1% C-CoCrFeMnNi high-entropy alloy additively manufactured by selective laser melting, Mater. Res. Lett. 8 (2020) 1–7.
[50] R. Chen, G. Liu, P. Wu, Y. Zhang, X. Wang, Y. Shen, Hetero-deformation induced (HDI) stress measurement from the plastic dissipation in the hysteresis loops, Mater. Res. Lett. 13 (2025) 248–255.
[51] T.J. Jang, J.-H. Baek, J.-Y. Suh, A. Zargaran, S.S. Sohn, Microstructural origin of the superior strength–ductility synergy of γ′-strengthened high-entropy alloy with heterogeneous grain structure and discontinuous precipitation configuration, J. Mater. Res. Technol. 27 (2023) 984–999.
[52] S.I. Hong, C. Laird, Mechanisms of slip mode modification in FCC solid solutions, Acta Mater. 38 (1990) 1581–1594.
[53] T.J. Jang, Y.N. Lee, Y. Ikeda, F. Körmann, J.-H. Baek, H.-S. Do, Y.T. Choi, H. Gwon, J.-Y. Suh, H.S. Kim, Compositive role of refractory element Mo in improving strength and ductility of face-centered-cubic complex concentrated alloys, Acta Mater. 255 (2023) 119030.
[54] G.B. Olson, M. Azrin, Transformation behavior of TRIP steels, Metall. Trans. A 9 (1978) 713–721.
[55] Y. Li, R.K. Nutor, Q. Zhao, X. Zhang, Q. Cao, S. Sohn, X. Wang, S. Ding, D. Zhang, H. Zhou, Unraveling the deformation behavior of the Fe45Co25Ni10V20 high entropy alloy, Int. J. Plast. 165 (2023) 103619.
[56] M.J. Sohrabi, H. Mirzadeh, S. Sadeghpour, R. Mahmudi, Grain size dependent mechanical behavior and TRIP effect in a metastable austenitic stainless steel, Int. J. Plast. 160 (2023) 103502.
[57] M.J. Sohrabi, H. Mirzadeh, S. Sadeghpour, R. Mahmudi, Explaining the drop of work-hardening rate and limitation of transformation-induced plasticity effect in metastable stainless steels during tensile deformation, Scr. Mater. 231 (2023) 115465.
[58] W. Mao, S. Gao, W. Gong, T. Kawasaki, T. Ito, S. Harjo, N. Tsuji, Martensitic transformation-governed ldeformation enables large ductility and late-stage strain hardening in ultrafine-grained austenitic stainless steel at low temperatures, Acta Mater. 278 (2024) 120233.